

SUPPORTING INFORMATION

Evolution of Aggregate Structure in Solutions of Anionic Monorhamnolipids: Experimental and Computational Results

Ryan J. Eismin,¹ Elango Munusamy,¹ Laurel L. Kegel,¹ David E. Hogan,²

Raina M. Maier,² Steven D. Schwartz,¹ and Jeanne E. Pemberton^{1}*

¹Department of Chemistry and Biochemistry

and

²Department of Soil, Water and Environmental Science

University of Arizona, Tucson, AZ 85721

*Author to whom correspondence should be addressed: pembertn@email.arizona.edu

Contents

I.	Additional Experimental Methods and Materials	
A.	Composition of Monorhamnolipid Mixture	S3
B.	Silanization Procedure for Fluorescence Cuvettes	S4
II.	Surface Tensiometry of Monorhamnolipid Solutions	S4
III.	Dynamic Light Scattering Results	S5
IV.	Fluorescence Spectroscopy for Determining N_{agg}	
A.	Solution Emission Spectra for Pyrene and Prodan	S6
B.	Emission Spectra of Prodan in mRL Aggregates at pH 4.0	S7
C.	Method of Turro and Yekta	S7
D.	Association of Fluorescent Probes with Micelles	S9
E.	Time Resolved Fluorescence Results and k_q/k Values	S11
F.	Polydispersity of Aggregates from Fluorescence Quenching	S11
V.	Molecular Dynamics Simulations	
A.	Force Field Parameter Development	S13
B.	Method Validation on SDS	S15
C.	Molecular Dynamics Simulations Performed	S16
D.	Micelle Shape (Eccentricity) from MD Simulations	S17
E.	Accessible Surface Area (ASA) from MD Simulations	S17
F.	Radial Density Plots of Micellar Components	S18
G.	Alkyl Chain Conformations in Aggregates	S19
H.	Gas Phase Structure of Rha-C10-C10	S19

I.	Interfacial Na ⁺ distribution	S20
VI.	References	S22

I. Additional Experimental Methods and Materials:

A. Composition of Monorhamnolipid Mixture. LC-MS² was done on the native monorhamnolipid mixture from *P. aeruginosa* ATCC 9027 to allow identification of composition. The major congener list for one batch of monorhamnolipids from ATCC 9027 is included in the table below with the remaining 2% consisting of trace amounts of 31 other uniquely identifiable congeners. As noted elsewhere, these abundances exhibit considerable variability both between bacterial strains as well as batch-to-batch variability within a single strain.

Congener	Abundance
Rha-C8-C10	5.5%
Rha-C10-C8	3.6%
Rha-C8-C12	7.7%
Rha-C10-C10	72%
Rha-C12-C8	5.1%
Rha-C10-C12:1	1.1%
Rha-C10-C12	2.6%
Rha-C12-C10	1.1%

One important difference to note about the native rhamnolipid mixtures produced by microorganisms is that they can exhibit considerable batch-to-batch variability from the intrinsic variability in metabolism of different colonies of bacteria. It is this intrinsic variability that leads to the range of abundances for the main Rha-C10-C10 congener in these mixtures.

B. Silanization Procedure for Fluorescence Cuvettes. To prevent mRL adsorption to the glass walls, fluorescence cuvettes were silanized with a fluoro-terminated silane. Fluorescence cuvettes were pretreated with a cleaning solution consisting of 4:1:1 (v/v) water, 30% (v/v) hydrogen peroxide and concentrated NH_4OH (14.5 M) by boiling for at least 45 min, followed by thorough rinsing with Milli-Q water. They were then dried under vacuum for 2-3 h at 120 °C. Next, the silanizing solution was made in an environmental control box under constant Ar and N_2 flow to eliminate water contamination by mixing dry toluene 97.5% (v/v), dry (tridecafluoro-1,1,2,2-tetrahydrooctyl) triethoxysilane 2% (v/v), and dry pyridine 0.5% (v/v) for 10 min and immediately added to the cuvettes, which were filled for an even coating. The solution was allowed to sit in the cuvette for 4 h. The glassware was rinsed with several aliquots of dry toluene, followed by several aliquots of absolute ethanol. The cuvettes were placed under vacuum for 12 h at 100 °C to allow the coating to cure.

II. Surface Tensiometry of Monorhamnolipid Solutions

Surface tensiometry of the native mRL mixture from *P. aeruginosa* ATCC 9027 was performed to determine the critical aggregation concentration (CAC). Results are shown in **Figure S1** for aqueous solutions at pH 8.0, 7.0 and 6.8.

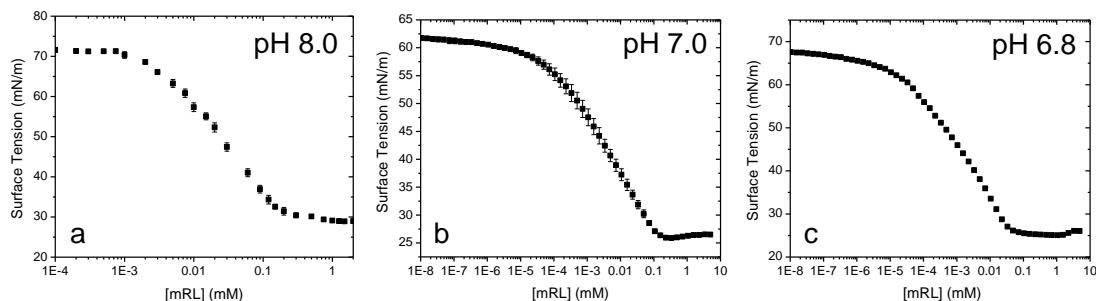


Figure S1. Surface tension as a function of native mRL mixture concentration in a) aqueous 10 mM phosphate buffer at pH 8.0, b) 0.063 M KH_2PO_4 /0.037 M NaOH at pH 7.0, and c) pH 6.8 in a minimal amount of NaOH. Error bars from triplicate measurements are present but smaller than the symbols shown in the plot.

III. Dynamic Light Scattering Results

DLS was used to identify aggregate populations and to estimate their sizes in solutions above the CMC. **Figure S2** shows representative DLS intensity and number distributions in mRL solutions of 5 and 20 mM. **Figure S3** shows the behavior of the three aggregate populations observed as a function of mRL concentration. **Figure S4** shows the polydispersity index calculated from the DLS data using the methods of cumulants analysis.^{1,2}

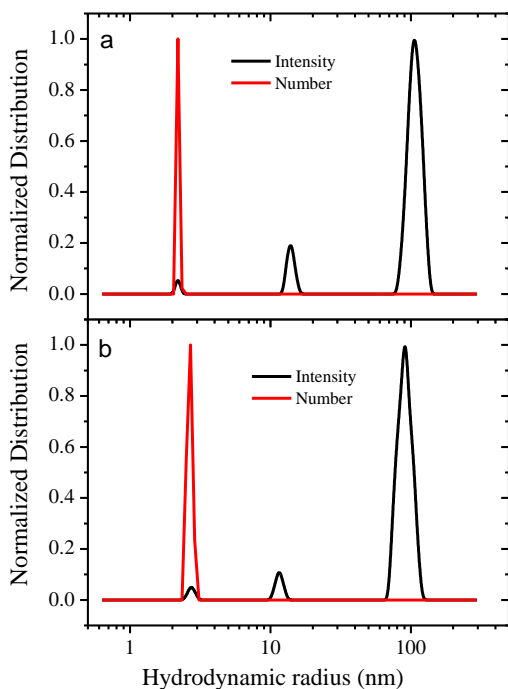


Figure S2. Representative normalized number (red) and intensity (black) distributions from DLS for a) 5 mM and b) 20 mM native mRL.

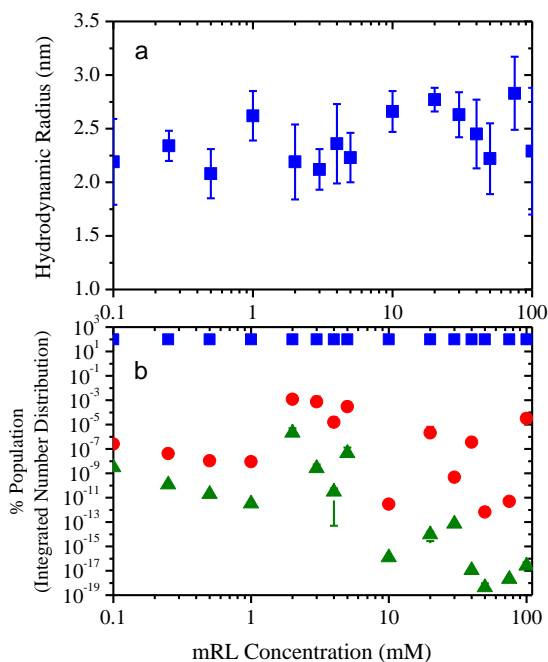


Figure S3. a) Dependence of hydrodynamic radii of pre-micelles/micelles on mRL concentration at pH 8 in 10 mM phosphate buffer. b) % of aggregate population from integrated number distributions for micelles (blue) and vesicles (red and green).

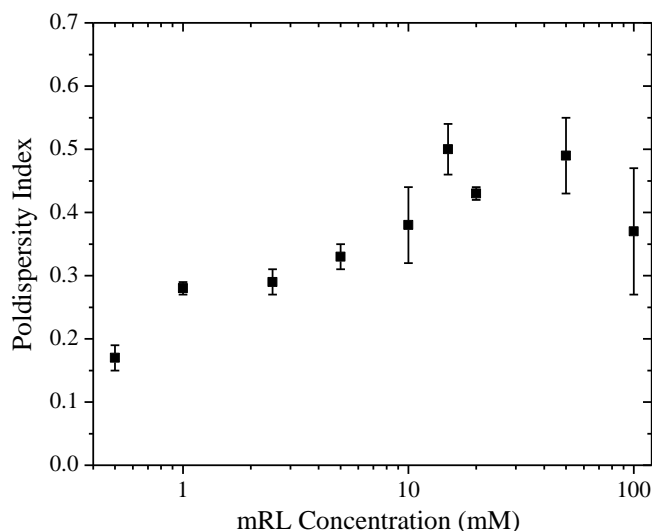


Figure S4. Polydispersity index as a function of mRL concentration. Values calculated from the DLS average correlation function data using the method of cumulants analysis.

IV. Fluorescence Spectroscopy for Determining Aggregate Type and N_{agg}

A. Solution Emission Spectra for

Pyrene and Prodan. An emission spectrum of pyrene in ethanol is shown in **Figure S5**. Peak III increases in intensity relative to peak I in more nonpolar environments.³ An emission spectrum of prodan in ethanol is also shown in **Figure**

S5. The emission maximum for prodan is known to shift toward the blue in more nonpolar environments.⁴

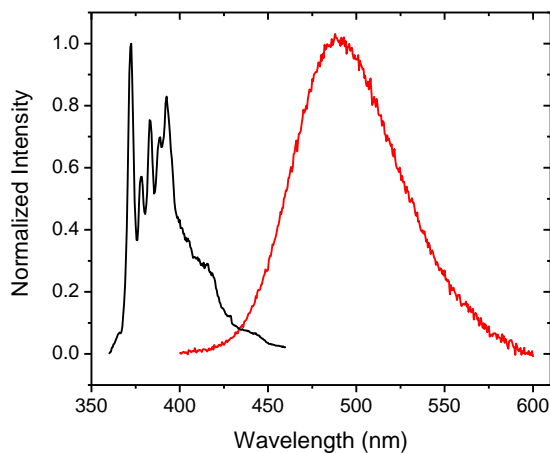


Figure S5. 250 nM pyrene (black) and prodan (red) emission spectra in ethanol. Excitation at 340 nm.

B. Emission Spectra of Prodan in mRL Aggregates at pH 4.0.

Fluorescence spectra of prodan in mRL aggregates at pH 4.0 as a function of mRL concentration is shown in **Figure S6**. The peak at ~445 nm indicative of lamellar phases⁵ clearly dominates the

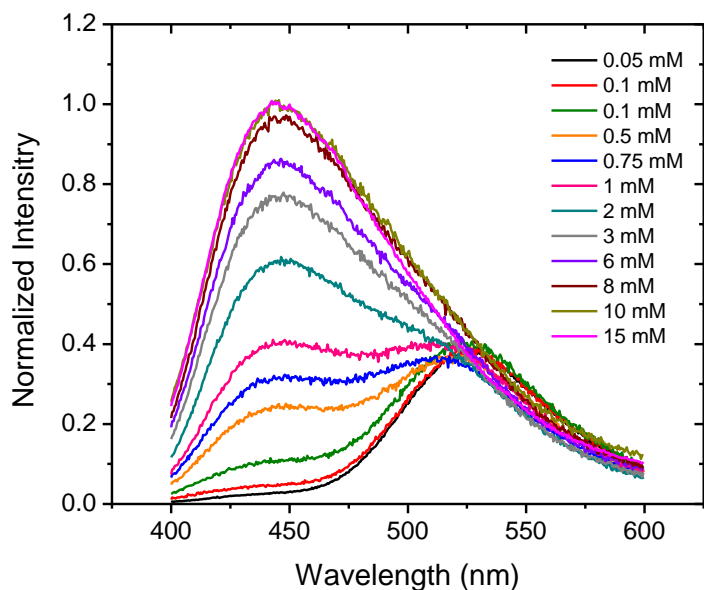


Figure S6. 250 nM prodan emission spectra as a function of mRL concentration at pH 4.0 . Excitation at 340 nm.

spectra at pH 4.0 with little micellar aggregates evident in contrast to dominance of the micellar structure in the spectra at pH 8.0 as described in the main body of the text.

C. Method of Turro and Yekta. The method of Turro and Yekta for the steady-state fluorescence determination of N_{agg} requires specific assumptions to be met: 1) the probe and quencher must follow a Poisson distribution within the micelle,^{6,7} 2) the dynamic quenching rate constant (k_q) must be large relative to the fluorescence lifetime of the probe (k_0); k_q/k_0 should be >10 ,^{8,9} 3) probes and quenchers must have a high affinity for the micelle interior relative to the aqueous environment, 4) micelles are relatively monodisperse and small ($N_{\text{agg}} < 500$), and 5) P migration from aggregates is minimal.⁷ Pyrene and benzophenone (BP) have been used many times to determine N_{agg} with other surfactants.

Poisson statistics can be used to understand the probability (P_n') of finding n quenchers associated with a given micelle:⁷

$$P_n' = \frac{\langle Q \rangle^n}{n!} e^{-\langle Q \rangle} \quad (\text{S1})$$

where $\langle Q \rangle = [Q]/[M]$ and n is the number of quenchers per micelle. For $n=1$ and $[Q]/[M] < 2$, the probability of finding no more than one quencher per micelle approaches unity. If a probe fluoresces only when it occupies a quencher-free micelle, the probability of finding no quenchers per micelle can be used (equation S2) to relate the fluorescence intensities measured in the presence of quencher (I) and without quencher (I_0) to micelle and quencher concentration, $[M]$ and $[Q]$, respectively.

$$P_0' = \frac{I}{I_0} = e^{-\frac{[Q]}{[M]}} \quad (\text{S2})$$

Micelle concentration can be related to aggregation number through:

$$[M] = \frac{[S] - [\text{free monomer}]}{N_{agg}} \quad (\text{S3})$$

where $[\text{free monomer}]$ is the concentration of free surfactant monomers in solution, which is equal to the critical micelle concentration (CMC) or critical aggregation concentration (CAC) for all concentrations beyond the CMC/CAC. Combining equations (S2) and (S3) gives the Stern-Volmer equation (S4), which can be plotted to derive N_{agg} .

$$\ln \frac{I_0}{I} = [Q] \frac{N_{agg}}{[S] - \text{CMC}} \quad (\text{S4})$$

D. Association of Fluorescent Probes with Micelles. The association constant of a fluorescent probe with the interior of a micelle (K_p) can be independently determined using a method developed by Quina and Toscano.¹⁰ For a probe with a high affinity for the interior of the micelle and whose fluorescence intensity changes due to a change in polarity of its microenvironment, increasing the micelle concentration allows more probe uptake, thereby changing the total fluorescence intensity. The relationship between the change in intensity with increasing micelle concentration is given by:¹⁰

$$\frac{I_\infty - I_0}{I_t - I_0} = 1 + \frac{1}{K_p[M]} \quad (\text{S5})$$

where I_∞ , I_0 , and I_t are the fluorescence intensities at high (i.e. approaching infinite) micelle concentration, zero micelle concentration, and at a given micelle concentration, respectively. For a surfactant with N_{agg} values that are known or can be estimated using Tanford's methods,¹¹ $[M]$ can be calculated using equation (S3). In this case, K_p can be estimated from the slope of a plot of $I_\infty - I_0 / I_t - I_0$ versus $1/[M]$, **Figure S7**, with N_{agg} estimated by Tanford's method and the assumption that N is constant over the studied $[S]$ range. K_p estimated from this work is $(1.94 \pm 0.08) \times 10^4 \text{ M}^{-1}$.

As discussed in the main body of the text, the association constant (K_Q) of a quencher for the micelle interior can be determined using the method of Tachiya that more fully describes the fluorescence quenching behavior according to¹²:

$$\ln \frac{I_0}{I} = \frac{[Q]}{\left\{ \frac{([S] - CAC)}{N_{agg}} + 1/K_Q \right\}} = n \quad (\text{S6})$$

$$\alpha = \frac{1}{\left(\frac{[S] - CAC}{N_{agg}} + 1/K_Q \right)} \quad (S7)$$

In fact, the method of Turro and Yekta is an approximation in which the $1/K_Q$ term is assumed to be negligible. Defining α to be the slope of a plot of n versus $[Q]$, a plot of $1/\alpha$ vs. $[S]-CAC$ (**Figure S8**) can be used to estimate K_Q and N_{agg} from the intercept and slope of a fit of the linear portion of the values, respectively. These results suggest that at concentrations <7.5 mM, the K_Q value for BP is lower than that for concentrations >7.5 mM, as would be expected for relatively loosely-packed pre-micellar structures. For mRL concentrations >7.5 mM, fully formed micelles exist which then exhibit a continual slight increase in N_{agg} with increasing mRL concentration. Further evidence for the formation of true micelles at mRL concentrations >7.5 mM comes from the data shown in Figure S5; tangents to this curve for mRL concentrations near 10 mM begin to have smaller intercepts, indicating larger values of K_Q for BP as would be expected for true micelles. In this region >7.5 mM, the smallest value of K_Q determined is $1.47 \times 10^4 \text{ M}^{-1}$.

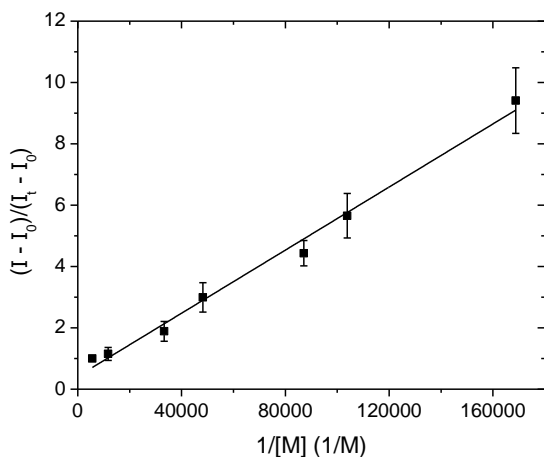


Figure S7. Fluorescence plot to determine the association constants of pyrene into native mRL micelles. All solutions held at pH 8.0/10 mM phosphate buffer. Slope = 5.14×10^{-5} , $R^2 = 0.989$.

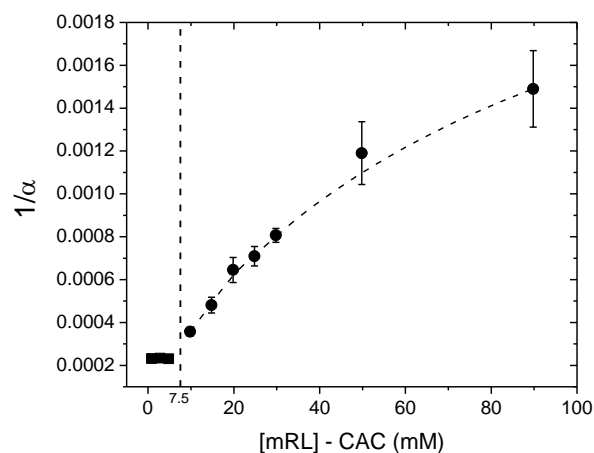


Figure S8. $1/\alpha$ values calculated from equations S6 and S7 as a function of mRL concentration. All solutions contained 250 nM pyrene with 0 to 300 μM BP in pH 8.0/10 mM phosphate buffer.

E. Time Resolved Fluorescence Results and k_q/k_0 Values. TCSPC curves of pyrene fluorescence decay in the absence (black) and presence (pink, blue, red) of benzophenone quencher at three different mRL concentrations are shown in **Figure S9**. These decay curves are fit to equations in the main text to determine k_q/k_0 ratios (shown in **Table S1**) and N_{agg} values.

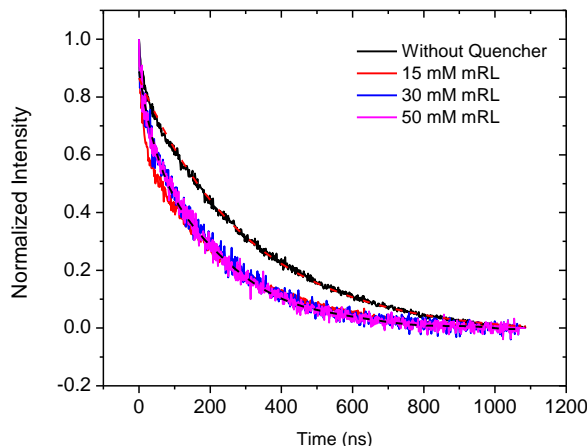


Figure S9. Representative TCSPC curves of pyrene in native mRL micelles quenched with BP. All solutions held at pH 8.0 in 10 mM phosphate buffer.

Table S2. Values of k_q/k_0 and k for different concentrations of mRL.

[mRL] (mM)	k_q/k_0	k (s^{-1})	τ_{res} (s)
1	1.6 ± 0.2	$6.8 (\pm 1.1) \times 10^{-4}$	$1.5 (\pm 0.6) \times 10^3$
3	1.9 ± 0.3	$6.9 (\pm 0.6) \times 10^{-4}$	$1.4 (\pm 0.3) \times 10^3$
5	3.3 ± 0.3	$4.5 (\pm 0.4) \times 10^{-4}$	$2.2 (\pm 0.2) \times 10^3$
10	13 ± 1	$3.5 (\pm 1.3) \times 10^{-4}$	$2.9 (\pm 0.7) \times 10^3$
15	26 ± 3	$2.8 (\pm 0.3) \times 10^{-4}$	$3.6 (\pm 0.2) \times 10^3$
30	25 ± 4	$2.8 (\pm 0.1) \times 10^{-4}$	$3.6 (\pm 0.1) \times 10^3$
50	27 ± 2	$1.2 (\pm 0.2) \times 10^{-4}$	$8.3 (\pm 0.1) \times 10^3$

F. Polydispersity of Aggregates from Fluorescence Quenching. In a system of aggregates with multiple populations (i.e. micelle and lamellar), the aggregation number varies as a function of $\langle Q \rangle = [Q]/([S] - CMC)$.¹³ If a system has a population that is polydisperse, the quencher will first load into aggregates with more total mass, the

lamellar aggregates,^{14,15} and then at higher $\langle Q \rangle$, quenchers will occupy aggregates with less total mass, here the micelles.¹³⁻¹⁵ By varying quencher concentration, a weighted average aggregation number ($N_{agg,w}$) can be calculated, and if significant polydispersity exists, then N_{agg} and $N_{agg,w}$ will differ. The basis of this relationship is described in more detail in the Supporting Information. This relationship can be experimentally determined by fitting the following relationship:¹³

$$N_{agg} = N_{agg,w} - \frac{\sigma^2 \langle Q \rangle}{2} + \frac{\xi \langle Q \rangle^2}{6} \quad (10)$$

where ξ is the skewness and σ is the standard deviation. Therefore, if σ is zero and $N_{agg,w} \approx N_{agg}$, then significant polydispersity does not exist. N_{agg} as a function of $\langle Q \rangle$ is shown in Figure S10a for a 15 mM native mRL solution. Although there is scatter in the data, N_{agg} does not significantly change with $\langle Q \rangle$, and fitting Figure S10a shows $\sigma \approx 0$.

To further evaluate polydispersity, the kinetics of the quenching rates can be extracted from the time resolved fluorescence measurements. If significant polydispersity exists, then

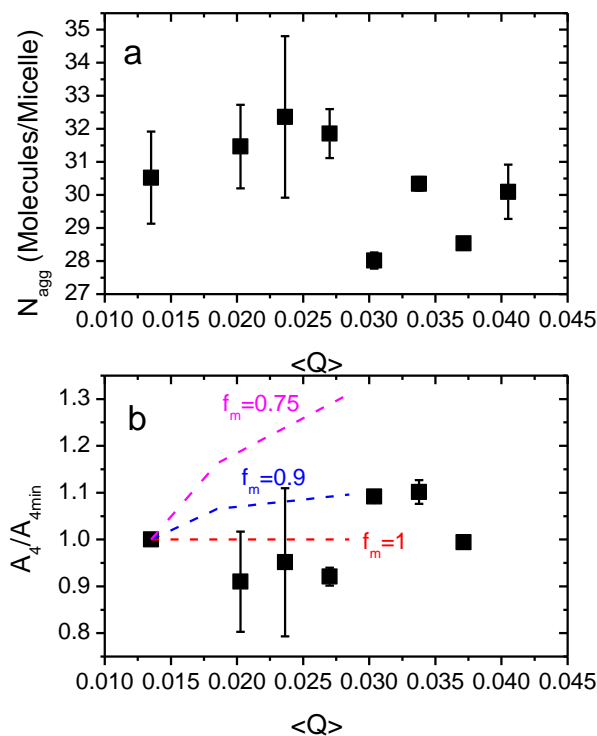


Figure S10. a) Average aggregation number, fit with dotted line, and b) A_3/A_{4min} vs. $\langle Q \rangle$ (black points) for a 15 mM mRL solution to evaluate polydispersity. Predicted f_m values of 0.75 (purple trace), 0.9 (blue trace), and 1 (red trace) correspond to 75%, 90%, and 100% micelles in solution, respectively. All solutions maintained at pH 8.0/10 mM phosphate buffer. Error bars represent standard deviations from three independently prepared samples.

the A_3 fitting term will vary with $\langle Q \rangle$ due to the loading of larger aggregates by quencher first.¹⁴⁻¹⁷ Figure S10b shows the $A_3/A_{3,\min}$ ratio as a function of $\langle Q \rangle$ as well as the fraction of micelles ($f_m = \text{number of micelles}/\text{total number of aggregates}$) to generate a quantitative value for polydispersity. This plot shows a fraction of micelles of ~ 1 across the entire mRL concentration range studied with very little change with $\langle Q \rangle$ indicating negligible polydispersity.

V. Molecular Dynamics Simulations

A. Force Field Parameter Development. Rhamnolipids (mRLs) are one class of molecules which have not been studied using Molecular Dynamics (MD) simulation methods. Therefore the Force Field (FF) Parameters are not yet published for this molecule. In the present study we have developed FF parameters based on CHARMM. We have utilized ParamIT¹⁸, a toolkit for molecules parameterization within CHARMM/CGenFF protocol. This toolkit can be implemented in VMD and aids the parameterization of small molecules within CHARMM general force field approach. It is interfaced to Gaussian09 for quantum chemical (QC) calculations and the CHARMM program for molecular mechanical (MM) calculations. The algorithm for parameterization within the CGenFF approach has distinct steps and in the majority situations the same steps are used for most of the parameterized molecules. (1) The first step is to create an equilibrium geometry for the molecule of interest. It is optimized with MP2/6-31G* if the molecule is neutral and MP2/6-31+G* if it is negatively charged. This geometry is used for generation of initial topology, for frequency calculations and for charge optimization. (2) The next step is to obtain initial topology/parameters. The

CHARMM stream file can be generated using the ParamChem web-service¹⁹. ParamChem creates a molecule topology and parameters based on the analogy between parts of the molecule of interest and already parameterized molecules from its database. Because ParamChem generates parameters based on analogy, it fails in case if certain parts of molecule are unknown. We encountered this situation with the rhamnolipid. When ParamChem creates molecule parameters it assigns a penalty score for each parameter. This score indicates the quality of suggested value, low score means that there is a good match between this part of the molecule and parameterized molecules in database and no further refinement is needed. Medium and high penalty score means that this parameters are needed to be reoptimized. In real life, ParamChem might fail to provide any topology and one must create an initial CHARMM stream file manually using the Initial Topology Generation VMD plug-in and Parameter Browser. (3) The next step is to optimize charge. In CHARMM and CGenFF the atomic partial charges are optimized against the quantum chemical dipole moments and the hydrogen bond energies of the parameterized molecule and a water molecule. When calculating hydrogen bond energies of the parameterized molecule and a water molecule, one should consider water as an acceptor of hydrogen bond as well as donor of hydrogen bond. Then we assign initial partial charges. The charge groups were defined according to the functional groups involved in the molecule. Initial charges can be set manually by analogy, automatically by analogy or set to the electrostatic potential derived charge. We can optimize the charges with the Charge Fit Plug-In. The main idea is to be able to simultaneously see the charge distribution and the resulting properties of the molecule and how they relate to quantum chemical results. The properties include the hydrogen bond energies, distances

in the complexes with water and the molecule dipole moments. (4) The next step is to optimize bond lengths, angles and dihedral terms from equilibrium geometry and vibrational analysis. ParamIT provides a command line script which will perform MM minimization and vibrational analysis using the CHARMM program. It then automatically compares equilibrium internal coordinates and vibrational modes of the molecular mechanics and quantum chemical models. (5) The next and final step is the very important dihedral optimization. A dihedral fitting plug-in to VMD is a tool aiding the parameterization of dihedral terms. It uses the CHARMM program to do the scan of the molecular mechanics model and it provides a graphical environment for manual fit along with capabilities for automatic fit. If the fit of dihedral term between quantum chemical and molecular mechanic models match well, then we could use the topology and parameters for molecular dynamics simulation. We were able to obtain a good set of parameters for monorhamnolipid that works well in terms of dihedral angles.

B. Method Validation on SDS. To validate the MD simulation methods used, they were applied to a well-studied surfactant system, sodium dodecyl sulfate (SDS). For a collection of 120 anionic SDS molecules with 120 Na⁺ in a 10 x 10 x 10 nm³ box of water, two micelles of ~60 SDS molecules each form as shown in **Figure S11**. This aggregation number of 60 is completely consistent with multiple measures of aggregation number for SDS reported in numerous papers in the literature,^{7,8} thus validating the MD simulation methods used here.

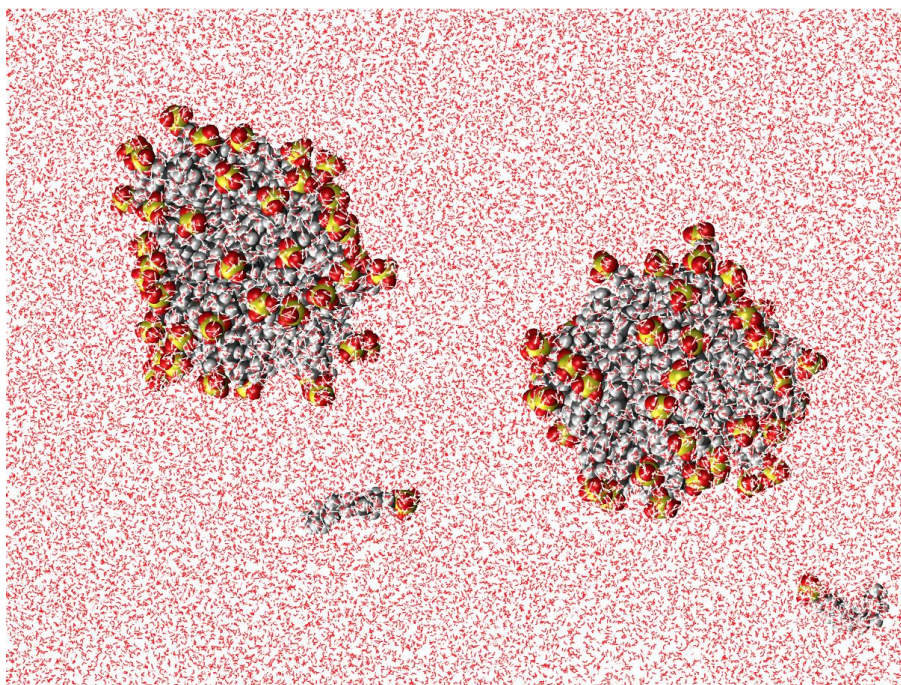


Figure S11. Results of MD simulation of 120 anionic SDS molecules with 120 Na⁺ in a 10 x 10 x 10 nm³ box of water. Two micelles of ~60 monomers each form.

C. Molecular Dynamics Simulations Performed.

Table S3 shows the list of systems studied in this work, comprising 10 to 100 molecules

Table S3. MD Simulation Information.

No. of Rha-C10-C10 Molecules	No. of Water Molecules	No. of Na ⁺ Ions	Total Atoms	Box Size (nm ³)	Effective Concentration (mM)	Simulation Time (ns)
10	31476	10	95258	10×10×10	17	27
20	31087	20	94921	10×10×10	33	36
25	30919	25	94832	10×10×10	42	38
30	30713	30	94629	10×10×10	50	33
40	30313	40	94259	10×10×10	66	28
70	29136	70	93218	10×10×10	118	34
80	28779	80	92977	10×10×10	133	41
100	28122	100	92666	10×10×10	166	36

of the most common congener in the native mRL mixture, the Rha-C10-C10, in their anionic state in a simulation box of size $10 \times 10 \times 10 \text{ nm}^3$ was used to solvate the Rha-C10-C10 molecules.

D. Micelle Shape (Eccentricity)

from MD Simulations. The shape of the micelle can be characterized by examining the eccentricity (e) as defined in the text. **Figure S12** shows the eccentricity as a function of simulation time for all micellar aggregates.

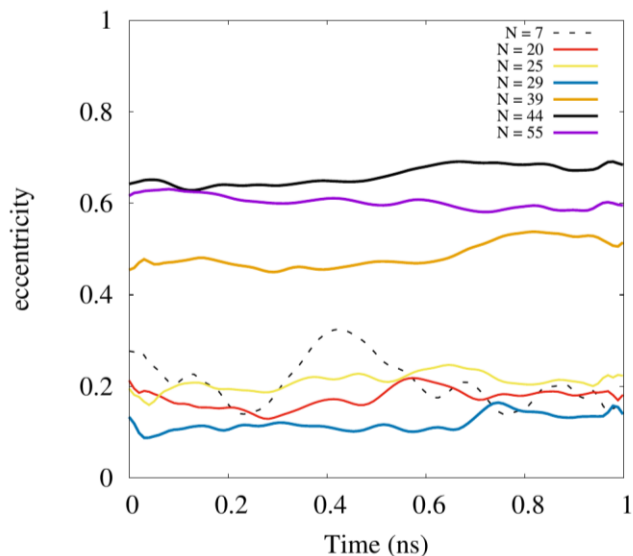


Figure S12. Eccentricity of the all the aggregates calculated for a period of 1 ns. The dotted lines correspond to pre-micellar aggregate and solid lines correspond to fully formed micellar aggregates.

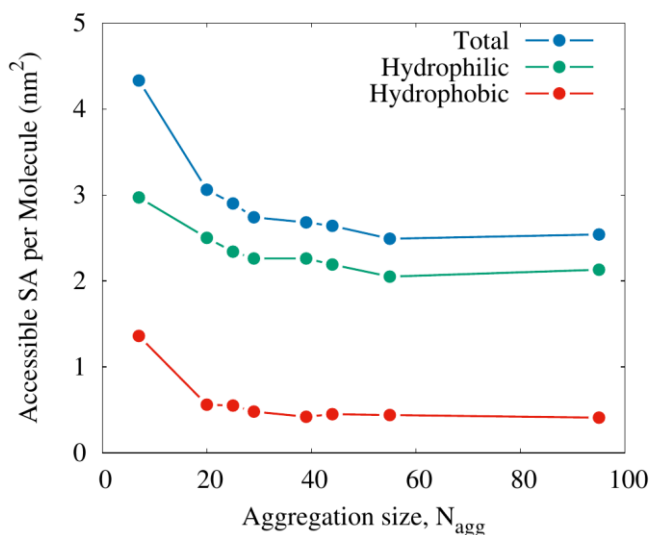


Figure S13. Accessible surface area per molecule of a theoretical water probe of all deprotonated mRL aggregates observed in the simulation.

E. Accessible Surface Area (ASA) from MD Simulations.

The ASA available to a 1.6 \AA diameter theoretical probe rolled across the surface of aggregates as a function of aggregate size is shown in **Figure S13**. Total ASA is shown in blue with hydrophobic and hydrophilic portions in red and green, respectively.

F. Radial Density Plots of Micellar

Components.

Molecular dynamics simulations indicate that aggregate of size $N = 20, 25$ and 29 are nearly spherical and aggregates of sizes $N = 39, 44$ and 55 are ellipsoidal. An attempt has been made to explain this variation in shape using radial density profile of various components of the system. The radial density profiles for $N=25, 39$ and 55 are given in **Figure S14**. For a spherical case, the density varies smoothly with single Gaussian-like densities compared to an ellipsoidal aggregate. For $N=25$, the profiles are relatively smooth, but for $N=44$ and 55 , the densities are broader indicating more ellipsoidal aggregate shapes. The growth of an ellipsoidal aggregate is limited by least in one dimension. This diameter of the aggregate along the limiting dimension does not exceed twice the length of the extended length of the tail group.²⁰ This is clearly seen from the radial

density profiles of water, where irrespective of the broadening of the curve, the density of water reaches 10 % of its total density at the same distance from the COM of the micelle.

This clearly supports the above statement.

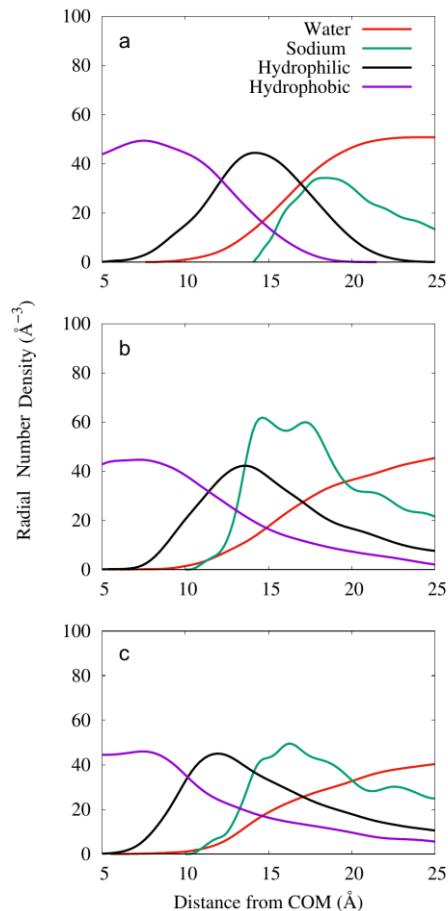


Figure S14. Radial number density of various components of the aggregate (a) $N=25$, (b) $N=39$ and (c) $N=55$ calculated along the radial direction from the micelle's COM. The plots are produced by counting the number of selected atoms that are within 0.1 \AA shells along the radial distance from the micelle's COM. The density of head groups and water molecules were multiplied by arbitrary factor for comparison.

G Alkyl Chain Conformations in

Aggregates.

In order to derive a possible relationship between the rhamnolipids tail extension length and the aggregation number, the length of the tail in all the aggregates sizes was calculated along the entire trajectory, **Figure S15**. The results show that the average tail length is ~ 6.8 Å irrespective of the size of the aggregates.

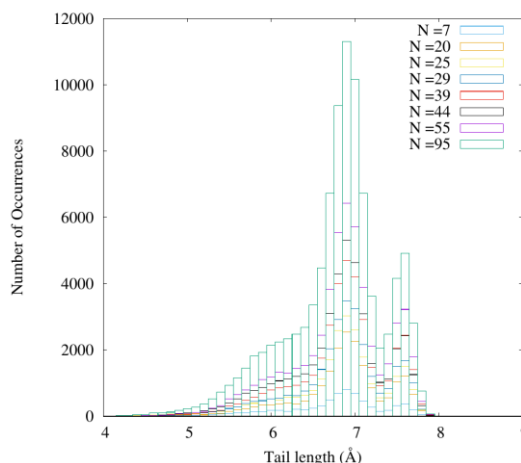
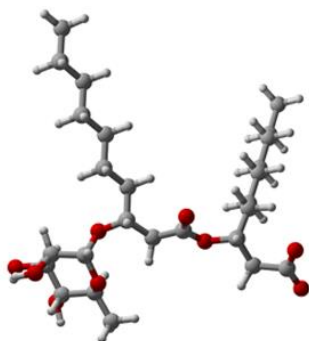


Figure S15. Average length of the hydrophobic tails in all of the aggregates. The plots are produced by calculating the length of the alkyl chain (distance between the terminal carbon atom and the sixth carbon from it) in all of the frames along the trajectory. The length of two alkyl chains are calculated independently and then an average is taken per monomer.

H. Gas Phase Structure of Rha-C10-

a



b

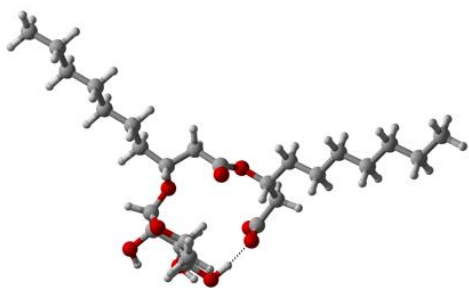


Figure S16. Optimized geometry of Rha-C10-C10 in the gas phase calculated by DFT(B3LYP) method using the basis set 6-31G*. a) The open conformation, which is 25.8 kcal/mol less stable than b) the closed conformation.

C10. Quantum chemical calculations on the various conformations of protonated Rha-C10-C10 were performed using Gaussian 09.²¹ Several orientations of the alkyl chain and intramolecular hydrogen bonding were considered. The density functional theory (DFT) gas phase calculation shows the most stable conformation as an intramolecularly hydrogen bonded structure where the oxygen atom of the terminal carboxylic group hydrogen bonds with a hydroxyl

group of the rhamnose ring. The open conformation where carboxylic group and rhamnose group are far apart was less stable than the folded conformation by ~ 25.8 kcal/mol. Corresponding conformations are presented in **Figure S16**.

I. Interfacial Na^+ distribution. In the present study, counter-ions are believed to play a crucial role in the size, shape, accessible surface area and radial density distribution of the micelles. The micelle-water interface is investigated to understand the connection between the micelle and the sodium counter-ions. The interaction between the micelle and Na^+ counter ions can be understood by investigating the distribution of Na^+ at the micelle-water interface (**Figure**

S15). This interaction is studied in detail by plotting the distribution of $\text{Na}^+ - \text{COO}^-$ pair distances (using the COM of the COO^-) of the Rha-C10-C10 molecules in aggregates. The % Na^+ that are within a given distance of any carboxylate group on the micelle is computed from the distribution data and shown in **Figure S17a**. It is important to mention that the distribution is similar for all aggregates, regardless of size; therefore, results for only the $N=25$ aggregate are shown for discussion. This figure shows that, within a distance of 5

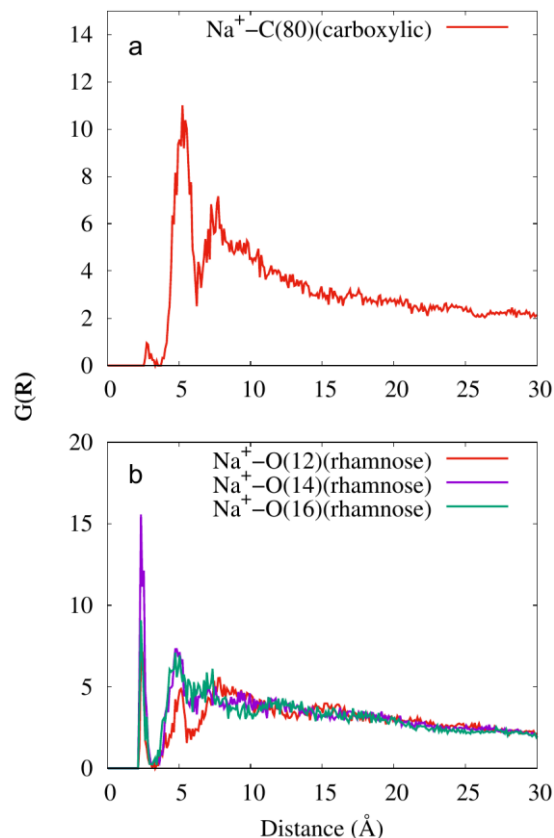


Figure S17. Radial pair distribution function of Na^+ with a) carbon (carboxylate group) b) hydroxyl oxygens (rhamnose group) of Rha-C10-C10.

<1%, with the % Na⁺ increasing slowly with distance in moving away from the carboxylate group. The presence of contact-ion pairs in this system is evident from the Na⁺ to carboxylate carbon radial distribution function (RDF, **Figure S17a**.) The first peak of the Na⁺-C80 (carboxylate) radial distribution function reaches a maximum at a distance of 5.25 Å. The slight ledge on the left side of this peak corresponds to regions of close contact between Na⁺ and carbon atoms of the carboxylate. This most likely occurs due to favorable electrostatic interactions with the two oxygen atoms of the carboxylate. In addition to the presence of contact-ion pairs, Na⁺ also interacts strongly with hydroxyl oxygens of the rhamnose group. The RDF plots shown in **Figure S17b** clearly indicate the presence of Na⁺ close to the rhamnose group. It is clear from these observations that Na⁺ interact with the charged COO⁻ group as well as the rhamnose group at the surface of the micelle. These results clearly indicate that Na⁺ is not bound to carboxylate groups most of the time. However, a close examination of the aggregate structures (**Figure S18**) reveals close association of Na⁺ with the carboxylate group as shown in **Figure S18b**. Na⁺ can also interact with hydroxyls on the rhamnose group (**Figure S18a**) and multiple carboxylate groups (**Figure S18c**). However, these interactions are rare and not observed for long periods of simulation.

These interactions may have a role in deciding conformation of Rha-C10-C10 molecules in the micelle.

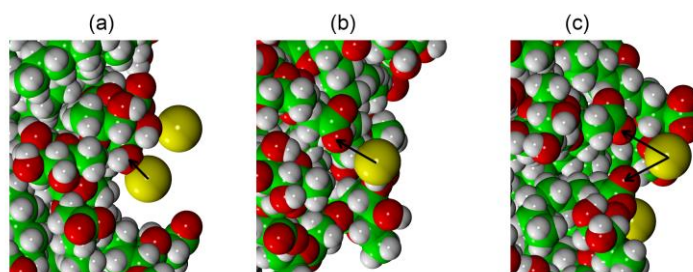


Figure S18. Representative structures of aggregates showing the presence of a) Na⁺ - OH interaction, b) Na⁺ - COO⁻ group interaction and c) Na⁺ - multiple COO⁻ group interaction. Yellow = Na⁺; green = C; red = O; grey = H.

VI. References

1. Koppel, D. E., Analysis of Macromolecular Polydispersity in Intensity Correlation Spectroscopy: The Method of Cumulants. *J. Chem. Phys.* **1972**, *57*, 4814–4820.
2. Berne, B. J.; Pecora, R., *Dynamic Light Scattering*. Krieger: Malabar, FL, 1990.
3. Basu Ray, G.; Chakraborty, I.; P., M. S., Pyrene Absorption can be Convenient Method for Probing Critical Micellar Concentration (cmc) and Indexing Micellar Polarity. *J. Colloid Interf. Sci.* **2006**, *294*, 248-254.
4. Parasassi, T.; Krasnowska, E. K.; Bagatolli, L.; Gratton, E., Laurdan and Prodan as Polarity-Sensitive Fluorescent Membrane Probes. *J. Fluoresc.* **1998**, *8*, 365-373.
5. Karukstis, K. K.; Duim, C. W.; Van Hecke, R. G.; Hara, N., Biologically Relevant Lyotropic Liquid Crystalline Phases in Mixtures of n-Octyl β -D-Glucoside and Water. Determination of the Phase Diagram by Fluorescence Spectroscopy. *J. Phys. Chem. B* **2012**, *116*, 3816-3822.
6. Turro, N. J.; Aikawa, M.; Yekta, A., Dynamics of Molecular-Oxygen in Micellar Solutions. *Chem. Phys. Lett.* **1979**, *64*, 473-478.
7. Turro, N. J.; Yekta, A., Luminescent Probes for Detergent Solutions - Simple Procedure for Determination of Mean Aggregation Number of Micelles. *J. Am. Chem. Soc.* **1978**, *100*, 5951-5952.
8. Alargova, R.; Kochijashky, I.; Sierra, M.; Zana, R., Micelle aggregation numbers of surfactants in aqueous solutions: A comparison between the results from steady-state and time-resolved fluorescence quenching. *Langmuir* **1998**, *14*, 5412-5418.
9. Tachiya, M., Application of Generating Function to Reaction-Kinetics in Micelles - Kinetics of Quenching of Luminescent Probes in Micelles. *Chem. Phys. Lett.* **1975**, *33*, 289-292.
10. Quina, F. H.; Toscano, V. G., Photophenomena in Surfactant Media - Quenching of Water-Soluble Fluorescence Probe by Iodide-Ion in Micellar Solutions of Sodium Dodecyl-Sulfate. *J. Phys. Chem.* **1977**, *81*, 1750-1754.
11. Tanford, C., Micelle Shape and Size. *J. Phys. Chem.* **1972**, *76*, 3020-3024.
12. Wu, S. Y.; Tachiya, M.; Yan, Z. N., An Improved Procedure for Determination of the Mean Aggregation Number of Micelles. *Spectrochim. Acta A* **2015**, *138*, 807-810.

13. Kegel, L. L.; Szabo, L. Z.; Polt, R.; Pemberton, J. E., Alkyl Melibioside and Alkyl Cellobioside Surfactants: Effect of Sugar Headgroup and Alkyl Chain Length on Performance. *Green Chem.* **2016**, *18*, 4446-4460.
14. Miller, D. D.; Evans, D. F., Fluorescence Quenching in Double-Chained Surfactants .1. Theory of Quenching in Micelles and Vesicles. *Journal of Physical Chemistry* **1989**, *93*, 323-333.
15. Miller, D. D.; Magid, L. J.; Evans, D. F., Fluorescence Quenching in Double-Chained Surfactants .2. Experimental Results. *Journal of Physical Chemistry* **1990**, *94*, 5921-5930.
16. Almgren, M.; Alsins, J.; Mukhtar, E.; Vanstam, J., Fluorescence Quenching Dynamics in Rodlike Micelles. *J. Phys. Chem.* **1988**, *92*, 4479-4483.
17. vonBerlepsch, H.; Stahler, K.; Zana, R., Micellar Properties of Sodium Sulfopropyl Alkyl Maleates in Aqueous Solution - A Time-Resolved Fluorescence Quenching Study. *Langmuir* **1996**, *12*, 5033-5041.
18. Simakov, N. A.; Wymore, T. *ParamIT*, National Resource for Biomedical Supercomputing: Pittsburgh Supercomputing Center, Pittsburgh, PA, 2012.
19. MacKerell, A.; Pamideghantam, S.; al., e. ParamChem. <http://www.paramchem.org/>.
20. Tanford, C., Thermodynamics of Micelle Formation - Prediction of Micelle size and size distribution. *Proc. Natl. Acad. Sci.* **1974**, *71*, 1811-1815.
21. Frisch, M. J.; Trucks, G. W.; Schlegel, H. B.; Scuseria, G. E.; Robb, M. A.; Cheeseman, J. R.; Scalmani, G.; Barone, V.; Mennucci, B.; Petersson, G. A.; Nakatsuji, H.; Caricato, M.; Li, X.; Hratchian, H. P.; Izmaylov, A. F.; Bloino, J.; Zheng, G.; Sonnenberg, J. L.; Hada, M.; Ehara, M.; Toyota, K.; Fukuda, R.; Hasegawa, J.; Ishida, M.; Nakajima, T.; Honda, Y.; Kitao, O.; Nakai, H.; Vreven, T.; Montgomery Jr., J. A.; Peralta, J. E.; Ogliaro, F.; Bearpark, M. J.; Heyd, J.; Brothers, E. N.; Kudin, K. N.; Staroverov, V. N.; Kobayashi, R.; Normand, J.; Raghavachari, K.; Rendell, A. P.; Burant, J. C.; Iyengar, S. S.; Tomasi, J.; Cossi, M.; Rega, N.; Millam, N. J.; Klene, M.; Knox, J. E.; Cross, J. B.; Bakken, V.; Adamo, C.; Jaramillo, J.; Gomperts, R.; Stratmann, R. E.; Yazyev, O.; Austin, A. J.; Cammi, R.; Pomelli, C.; Ochterski, J. W.; Martin, R. L.; Morokuma, K.; Zakrzewski, V. G.; Voth, G. A.; Salvador, P.; Dannenberg, J. J.; Dapprich, S.; Daniels, A. D.; Farkas, Ö.; Foresman, J. B.; Ortiz, J. V.; Cioslowski, J.; Fox, D. J. *Gaussian 09*, Gaussian, Inc.: Wallingford, CT, USA, 2009.